# Modeling Stress-Enhanced Photo-Degradation in Amorphous Glassy Polymers

Keven Alkhoury,[†‡] Laurence Brassart,[††] and Shawn A. Chester[‡*]

[†]School of Engineering
Brown University
184 Hope Street, Providence, RI 02906 USA

[‡]Mechanical Engineering
New Jersey Institute of Technology
Newark, NJ 07102 USA

[††] Department of Engineering Science
University of Oxford
Oxford OX1 3PJ, United Kingdom

May 5, 2026

**Abstract**

The emergence of renewable, degradable polymers in everyday applications necessitates the prediction of their mechanical behavior during service. In a recent contribution, Alkhoury et al. (2024) characterized changes in microstructural and mechanical behavior resulting from stress-enhanced photo-degradation of cellulose acetate, a renewable and degradable glassy amorphous polymer used in various consumer products. In this work, we complement the existing set of experiments and develop a thermodynamically consistent constitutive model informed by both micro- and macro-scale

*Corresponding author: shawn.a.chester@njit.edu

information. The outcome of this work enables the prediction of the mechanical behavior of photo-degrading glassy amorphous polymers while subjected to stresses. This can help engineers design sustainable devices while ensuring product integrity.

Keywords: Constitutive behavior; Degradable polymers; Renewable polymers; Stress-enhanced photo-degradation; Stress-enhanced UV degradation.

# 1 Introduction

Modern societal trends are focused on replacing petroleum-derived polymers with sustainable polymers with similar performance (Eerhart et al., 2012; Zhu et al., 2016; Elsawy et al., 2017; Nakajima et al., 2017; Asgher et al., 2020; Hayes et al., 2022; Singh et al., 2022; Campbell et al., 2023). Since sustainable polymers are much more likely to be degradable, it is important to understand how quickly they break down under environmental conditions versus how well they maintain their structural and functional integrity during storage and application. For that reason, it is important to have constitutive models with the ability to capture the mechanics concurrently with the relevant chemical processes, such as degradation reactions.

While the modeling of the mechanics of polymeric materials undergoing chemical reactions is still at a relatively early stage of development, there exists substantial work in the existing literature. In recent years, numerous studies have focused on polymer hydrolysis, that is, the degradation of polymers in the presence of water. For instance, Vieira et al. (2014) developed a three-dimensional time-dependent model to simulate the performance of biodegradable structures undergoing large deformations, incorporating hydrolysis degradation. Bahrololoumi et al. (2020) modeled the effect of hydrolytic aging on mechanical quasi-static responses of rubber-like materials, exhibiting the Mullins effect and permanent set. Brassart and co-workers developed a thermodynamically-consistent continuum framework and constitutive model for coupled large deformation and hydrolytic degradation in

hydrogels (Pan and Brassart, 2022), and more recently extended this framework to incorporate hydrolytic degradation and viscoplasticity in glassy polymers (Pan et al., 2026).

Turning attention to thermal degradation, Gigliotti et al. (2011) characterized and modeled the local shrinkage strains and stresses induced by thermo-oxidation in composite materials at high temperatures. Konica and Sain (2021) presented a homogenized thermodynamically consistent constitutive model to predict high-temperature oxidation for fiber-reinforced polymer matrix composites undergoing large deformation. Bahrololoumi and co-workers developed models that address concurrent effects on cross-linked polymers, such as thermo-oxidation (Bahrololoumi et al., 2021), and thermal aging and cyclic fatigue (Bahrololoumi et al., 2022). Song and Zhong (2024) developed a constitutive model to elucidate the mechanical degradation of carbon fiber-reinforced polymer composites when subjected to direct current while simultaneously accounting for thermal degradation. Moreover, Shakiba and Najmeddine (Shakiba and Najmeddine, 2023; Najmeddine and Shakiba, 2024) presented physics and chemistry-based constitutive frameworks to predict the mechanical responses of thermo-chemically aged elastomers.

Moving onto photo-degradation, Ayoub and co-workers modeled the effect of photo-degradation on various polymers ranging from amorphous to semi-crystalline (Belbachir et al., 2010; Ayoub et al., 2020; Lamnii et al., 2021). Mohammadi et al. (2021) proposed a micro-mechanical model to describe the effects of temperature and UV radiation on the constitutive behavior of cross-linked elastomers. Najmeddine et al. (2022) presented a physio-chemically-based constitutive framework to predict the response of severely photo-oxidatively aged semi-crystalline polymers. In all of these cases, the focus was limited to photo-degradation under traction-free conditions. While some of these studies investigated the effect of photo-degradation on the underlying chemistry of the polymers of interest, to the best of the authors' knowledge, no work exists that simultaneously addresses both stress effects and the underlying chemistry.

In a recent contribution, Alkhoury et al. (2024) addressed this limitation by characteriz-

ing the microscopic chemical changes associated with stress-enhanced photo-degradation and examining their influence on the mechanical response of cellulose acetate, a degradable polymer used in various consumer products. Specifically, cellulose acetate was photo-degraded under (i) traction-free conditions, and (ii) under an applied stress. A key finding of that work is that upon photo-degradation, cellulose acetate undergoes microstructural changes due to UV irradiation, which affects its mechanical properties and is further affected by the applied stress. Consequently, the objective of this work is to complement the existing set of experiments reported in that work and to develop a thermodynamically consistent constitutive model that captures the experimental observations.

The remainder of this paper is organized as follows. In Section 2, we briefly overview the experimental procedure reported in Alkhoury et al. (2024) by providing some background, along with a summary of the results and a list of major assumptions that are crucial to laying the foundation for our model. In Section 3, we describe the active physical mechanisms responsible for changes in the constitutive behavior in photo-degrading cellulose acetate. In Section 4 we overview the continuum-level model, calibrate it in Section 5, and then use the model to study a boundary value problem in Section 6 to demonstrate its practicality. In Section 7, we provide concluding remarks.

# 2 Experimental background and results from the literature

In this section, we provide background and major assumptions, reproduced from our earlier work (Alkhoury et al., 2024). We also summarize the experimental results that are crucial to laying the foundation of our model.

## 2.1 Attenuation of light

As monochromatic light travels through a participating medium in a given direction, it is well known that its intensity attenuates, a phenomenon based on a physical observation, often called the Beer-Lambert Law (Lambert, 1760), which can be schematically described by Figure 1.

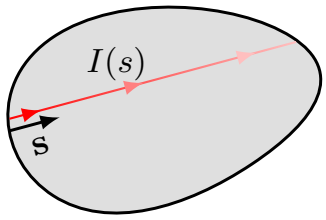


Figure 1: Schematic of a monochromatic light attenuation as it travels through a participating medium in a given direction denoted by the unit vector $\mathbf{s}$.

This phenomenon is commonly modeled in one dimension using

$$I(s) = I_0 \exp(-\beta s)\,, \tag{1}$$

where $I_0$ is the incident intensity, $\beta$ the attenuation coefficient, and $s$ is the path length. This attenuation is relevant to photo-degradation, as it results in an inhomogeneous intensity distribution through the sample's thickness during exposure. This results in an inhomogeneous degradation across samples, which must be mitigated as much as possible to ensure a clear interpretation of the experimental results.

Toward mitigating inhomogeneity in Alkhoury et al. (2024), the intensity of the incident light was first measured using a UV light meter (Omega-HHUV254SD), and the light intensity across cellulose acetate samples of relevant thicknesses was also measured, as shown in Figure 2. It was observed that the light was fully attenuated at a sample thickness of 254 $\mu$m, approximately twice that of the used samples. Next, the measurements were calibrated using (1), where Figure 2 shows a reasonable agreement between the "Beer-Lambert" model and

experimental results. Moreover, the parameters are tabulated in Table 1. For that reason,

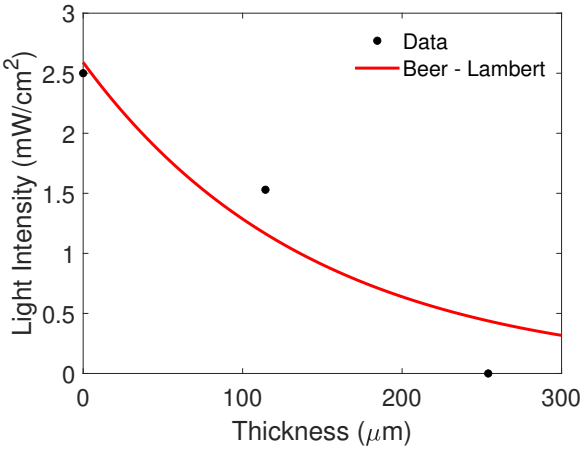


Figure 2: Light attenuation measurements along with the corresponding Beer-Lambert model for cellulose acetate samples of varying thicknesses.

| $I_0$ (mW/cm$^2$) | $\beta$ ($\mu$m$^{-1}$) |
|---|---|
| 2.59 | 0.007 |

Table 1: Beer-Lambert model parameters obtained from the calibration in Figure 2.

two UV sources were used, one from each side, as shown schematically in Figure 3, such that samples were exposed from both sides. Since light emanating from two independent sources with intensities $I_1$ and $I_2$ is incoherent, the combined intensity is given by $I(s) = I_1(s) + I_2(s)$ (Hecht, 2002). We further introduce an approximation based on an "average intensity"

$$\bar{I} = \frac{1}{h}\int_0^h I(s)\, ds\,, \tag{2}$$

where the "average intensity," $\bar{I}$, is assumed to be quasi-uniform, and results in a *nearly* homogeneous degradation across the thickness, as shown schematically in Figure 3. This was the first major assumption made in analyzing the experimental results. In the case that $\beta$ is a constant and does not vary in space, this leads to the simple result

$$\bar{I} = \frac{1}{h}\int_0^h I_0 \exp(-\beta s) + I_0 \exp\big(-\beta(h-s)\big) ds\,, \tag{3}$$

which in this case leads to an average intensity $\bar{I}$

$$\bar{I} = \frac{2I_0}{\beta h}\left[1 - \exp\left(-\beta h\right)\right] . \tag{4}$$

Lastly, exposure to UV light at a known intensity for a fixed amount of time is commonly referred to as "UV dose," often expressed in $\mathrm{mJ/mm^2}$. Accordingly, we take

$$\mathbb{D}(\mathbf{x}, t) \stackrel{\text{def}}{=} \int_0^t I(\mathbf{x}, \zeta) d\zeta \tag{5}$$

as the definition of UV dose. For the experiments, based on the average intensity assumption, that reduces to

$$\mathbb{D}(t) = \int_0^t \bar{I}(\zeta) d\zeta \, . \tag{6}$$

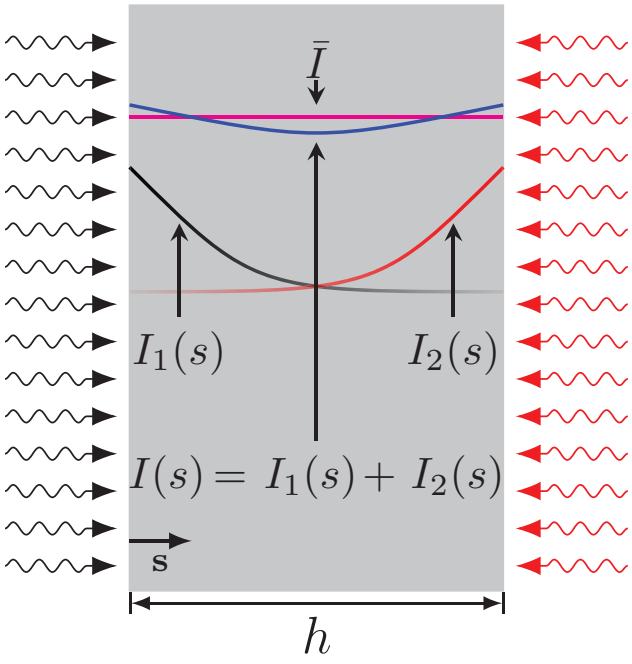


Figure 3: Schematic of light attenuation across the sample thickness and the approximated quasi-uniform "average intensity" $\bar{I}$.

## 2.2 Degradation mechanisms

All degradation experiments were conducted at a constant temperature of 27°C. In addition to that, since all degradation experiments occurred over a short period of time, any possible degradation due to physical aging, as well as thermal oxidation, was neglected, since both are expected to happen at a relatively longer time scale and much higher temperatures (Yousif and Haddad, 2013; Gardette et al., 2013; Rasselet et al., 2014). Furthermore, the mass of photo-degraded samples was measured using a balance (Sartorius Practum213-1S), and no measurable mass change was detected within the instrument accuracy (1 mg), corresponding to approximately 0.3%, for a 313 mg sample. Therefore, the second major assumption was that any measurable change in the micro- or macro-scale behavior of cellulose acetate is attributed solely to photo-degradation.

## 2.3 Virgin/baseline and degraded materials

When discussing materials undergoing degradation, two terms describing the state of the material are necessary to understand — virgin and degraded. Virgin material is a raw material without any prior degradation and loading history, serving the purpose of establishing a baseline behavior for comparison. Whereas degraded material is a material that has been subjected to degradation under different conditions (UV dose and stress), and is used to understand the effect of these conditions on the materials' response.

## 2.4 Photo-degradation apparatus and procedure

As reported in Alkhoury et al. (2024), prior to photo-degradation, commercially purchased amorphous cellulose acetate films were subjected to a stress relief heat treatment for 6 hours at a temperature of 135°C, followed by a slow cooling to room temperature overnight.[1] Then, tensile dog bone samples were extracted using an ASTM D638-V cutting die. The

[1]The cooling was uncontrolled in practice; the power was turned off, and the oven door was not opened until the next day.

nominal gauge section dimensions of samples were $\approx 9.52\,\text{mm}$ long, $\approx 3.14\,\text{mm}$ wide, and $\approx 0.114\,\text{mm}$ thick, though the exact dimensions of each sample were measured prior to testing for accuracy. The grip sections were then covered with tape, as schematically shown in Figure 4, to prevent any exposure to UV light and thus eliminate any possible degradation to these regions. Next, samples were gripped and exposed to UV light at a known intensity for a fixed amount of time, for the purpose of prescribing a known UV dose. Cellulose acetate samples were photo-degraded using two 20W UV lamps (Analytik Jena XX-20S) with a wavelength of $\lambda = 254$ nm, corresponding to UVC on the UV spectrum. Specifically, the 20W lamps were set at a standoff distance of $0.3\,\text{m}$, which led to an incident intensity of $I_0 = 2.5\,\text{mW/cm}^2$. In what follows, the average intensity $\bar{I} = 3.4316 \times 10^{-2}$ mW/mm$^2$ was used to compute the UV dose following (6). Moreover, the chosen exposure times were four (4), eight (8), and twelve (12) hours, resulting in UV doses of $\mathbb{D} = 494$ mJ/mm$^2$, $\mathbb{D} = 988$ mJ/mm$^2$, and $\mathbb{D} = 1482$ mJ/mm$^2$, respectively.

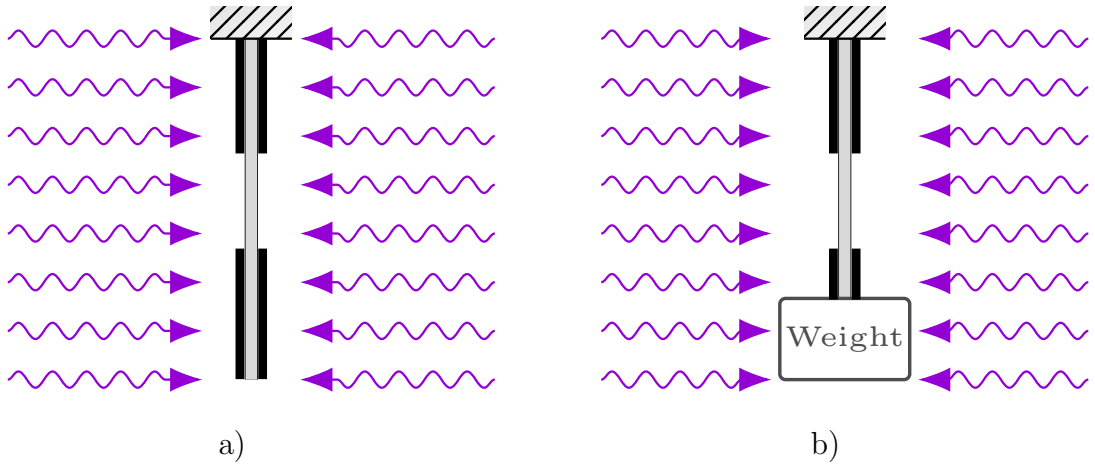


Figure 4: A schematic of the experimental setup used for a) traction-free degradation, and b) degradation under constant applied stress. Note that the UV light comes from both sides and that the grip section is taped, represented by the black in the figure, leaving only the gauge section open to UV light.

The degradation experiments in Alkhoury et al. (2024) were grouped into two categories: (i) traction-free degradation and (ii) degradation under a constant applied stress. For the traction-free degradation experiments, the samples were gripped from one end, hung under

their own weight, and exposed to UV light, as shown in Figure 4a. Those experiments provided a baseline behavior of photo-degrading cellulose acetate. For the degradation under constant applied stress, the samples were gripped from one end, and a known constant stress was applied from the other end, resulting in a constant tensile state of stress, as shown in Figure 4b. Those experiments probed the effect of stress on the mechanical behavior of photo-degrading cellulose acetate. The results from those experiments were reported in terms of engineering stress due to its simplicity, ubiquity, and acceptance by many other communities. We also note that any stress contribution due to the samples' weight was neglected in the traction-free degradation experiments as the samples typically weighed $\approx$ 0.025% of the smallest applied load (1.34 lbs), which is negligible. Moreover, five samples were used in each degradation experiment, and each degradation experiment was repeated at least once to ensure repeatability between the results. Lastly, photo-degraded samples were used to characterize the micro-scale and macro-scale response.

## 2.5 Summary of the experimental results

Key experimental results from Alkhoury et al. (2024) are summarized as follows. At the micro-scale, it was observed that an increase in the UV dose decreases the number average molecular weight $M_{\mathrm{n}}$, and the glass transition temperature $T_g$ (see Figure 5), without having any *significant* effect on the functional groups in cellulose acetate, regardless of the applied stress. This indicates that upon photo-degradation, the cellulose acetate backbone undergoes chain scission. At the macro-scale, cellulose acetate showed a rate-dependent elastic-plastic behavior with approximately linear strain hardening. It was observed that both the UV dose and applied stress affect the mechanical properties. The typical constitutive response, conducted at a nominal strain rate of $\dot{\varepsilon} = 10^{-3}$ s$^{-1}$, and reproduced from Alkhoury et al. (2024), is shown in Figure 6.

The mechanical properties of relevance were determined using the method shown in

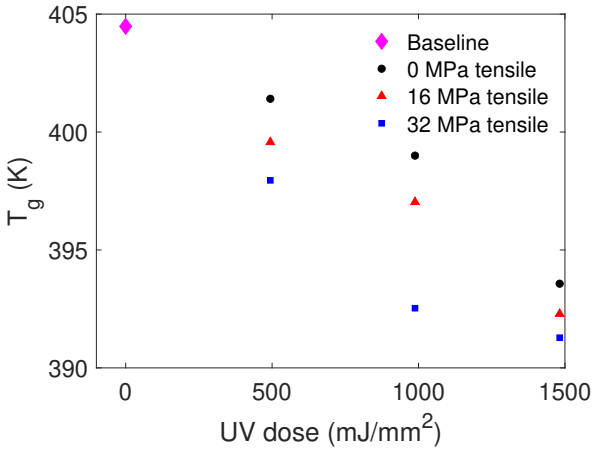


Figure 5: DSC results showing the $T_g$ for cellulose acetate subjected to different UV doses and applied stress. Note that the baseline plotted in magenta represents a virgin sample with no prior loading or exposure history.

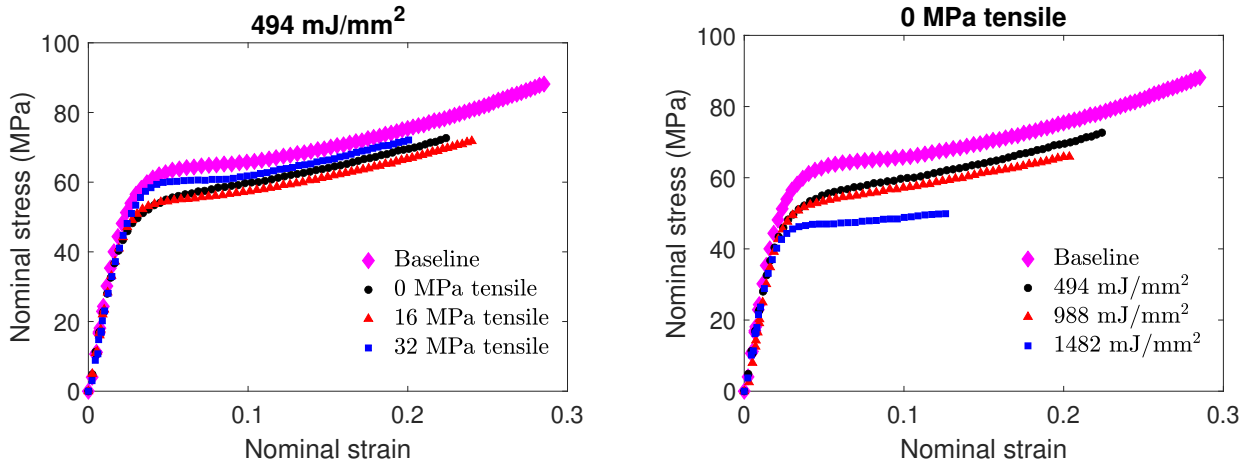


Figure 6: Typical uniaxial experimental results for load-unload tensile tests for cellulose acetate a) comparing the effect of the applied stress under the same UV dose, and b) comparing the effect of the UV dosage under the same applied stress.

Figure 7 and are reported in Figure 8.[2]

Starting with the elastic modulus reported in Figure 8a, we note that while some changes may be observed, the overall trend seems unaffected by both UV dose and applied stress. Next, the yield strength reported in Figure 8b shows a unique transitional behavior. When

[2]We note that since plasticity models are typically built upon true and not engineering quantities, the mechanical properties of relevance were also quantified using true quantities by imposing incompressibility restrictions on the uniaxial stress-strain curves (see Figure 7b), with the details provided in Appendix A.

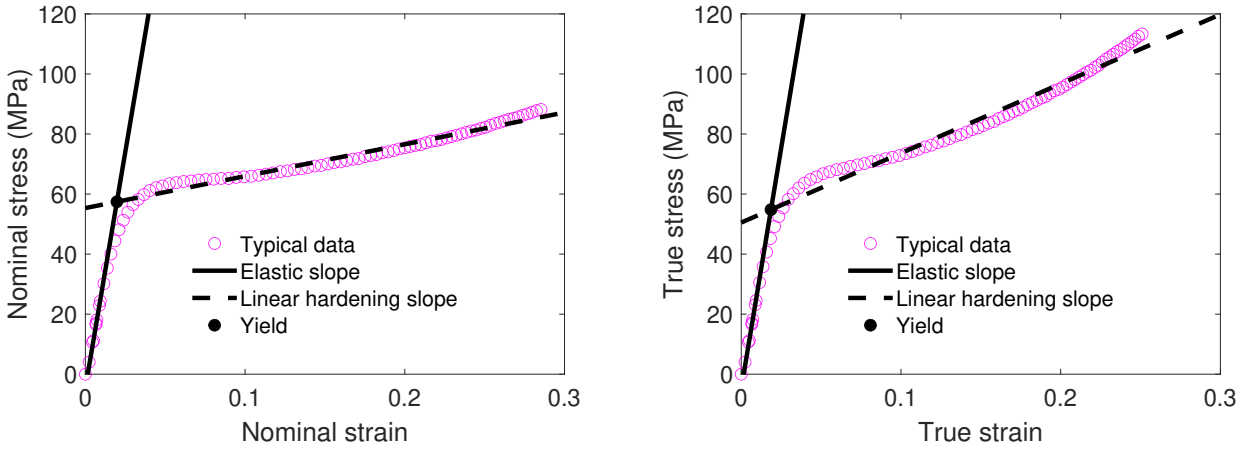


Figure 7: Schematic showing the method to determine the mechanical properties for a typical uniaxial experimental result using a) nominal stress-strain curves, and b) true stress-strain curves.

subjected to traction-free degradation, the yield strength decreases as the UV dose increases. On the other hand, when degradation occurs at 16 MPa tensile, the yield strength remains unchanged as the UV dose increases. Finally, when degradation occurs at 32 MPa tensile, the yield strength increases as the UV dose increases. Lastly, the hardening slope is obtained from both the nominal and true stress-strain curves reported in Figures 8c and d respectively, and decreases as the UV dose increases and decreases further with the addition of stress. In what follows, we relate changes in yield strength and hardening slope to ongoing physical mechanisms and use these findings to motivate our modeling effort.

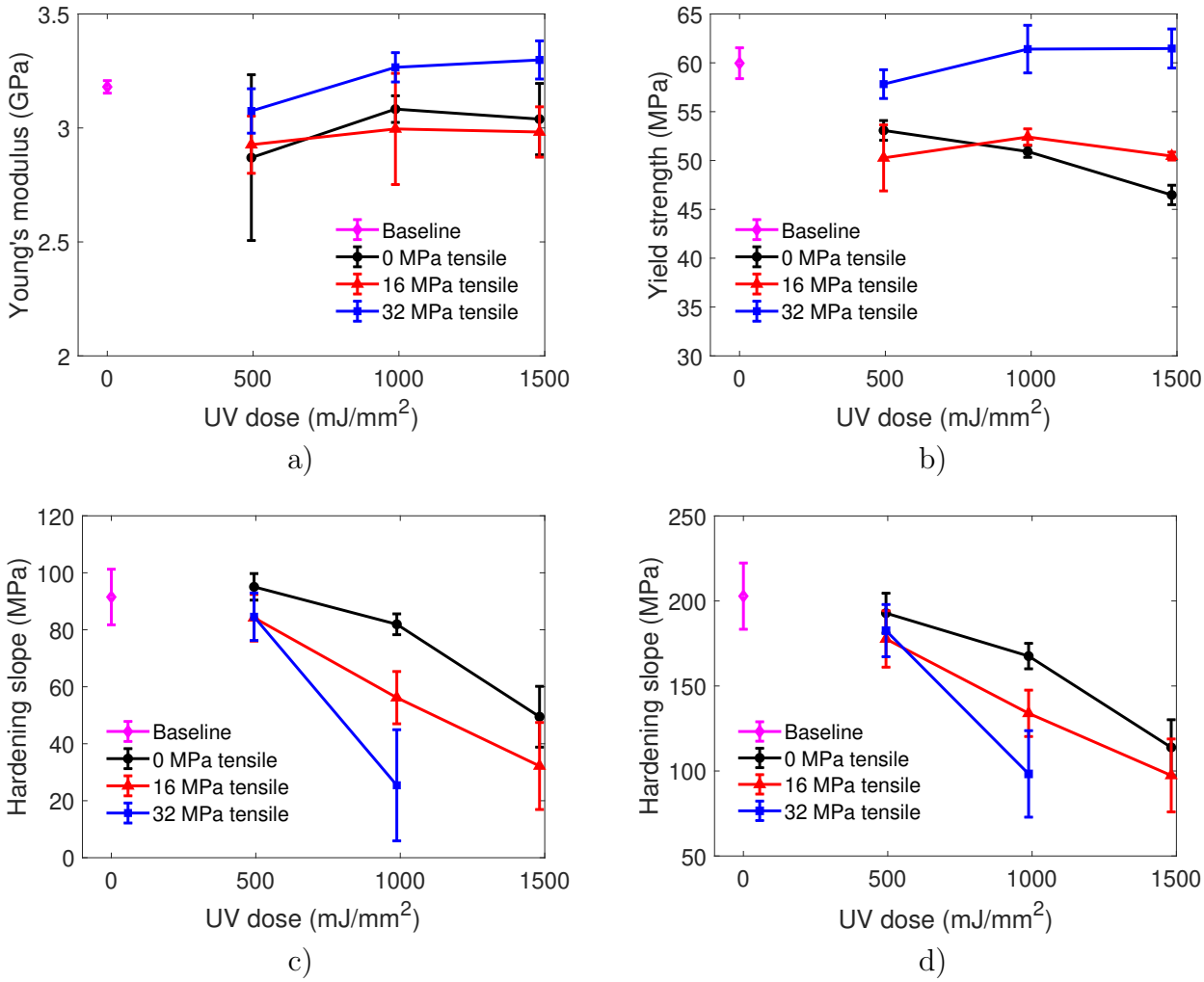


Figure 8: Mechanical properties calculated as an average from the uniaxial experimental results, a) Young's modulus, b) yield strength using true stress-strain, c) hardening slope obtained using engineering stress-strain, and d) hardening slope obtained using true stress-strain, for different applied stress and UV dose. Error bars indicate the standard deviation. Note that for a UV dose of 1482 mJ/mm$^2$ and an applied stress of 32 MPa tensile, the material was brittle, and did not show any hardening.

# 3 Potential physical mechanisms and corresponding internal variables

In this section, we describe the potential physical mechanisms responsible for changes in yield strength and hardening slope due to photo-degradation, and introduce the corresponding internal variables to support our modeling effort.

**The yield strength** reported in Figure 8b shows a unique transitional behavior. For degradation under traction-free conditions, the yield strength decreases as the UV dose increases, which is a typical behavior expected due to chain scission and the associated increase in free volume (Wu and Buckley, 2004). However, for degradation at 16 MPa tensile, the yield strength is unaffected by photo-degradation. This is due to the increased energy due to UV, which allows for strain hardening due to chain reorientation at stress levels below the yield, leading to an increased yield point, which has been observed in other contexts (Engqvist et al., 2016). Therefore, the decrease in yield due to scission is offset by the increase in yield due to chain reorientation under applied stress and UV. Additionally, for degradation at 32 MPa, the yield strength increases with increasing UV dose, suggesting that the increase in yield due to chain reorientation is more dominant than the decrease due to scission. Consequently, our model will include a dependence of the yield strength on two competing mechanisms, chain scission and chain reorientation induced by concurrent applied stresses and UV.

**The hardening slope** reported in Figures 8c and 8d shows a decrease with increasing UV dose due to chain scission. Furthermore, the hardening slope decreases further with increasing stress. The observed behavior suggests that during UV exposure, the application of stresses promotes chain scission, which in turn results in a "less-entangled" microstructure (Venkatesan and Basu, 2015; Narayan and Anand, 2021) and, therefore, the reduced significance of the intermolecular interactions.[3] Consequently, our model will include a dependence

[3]The entanglement density is known to be a key factor governing polymer mechanical behavior. Prior experimental (Van Melick et al., 2003) and computational (Hoy and Robbins, 2006) studies have shown that

of the hardening slope on the stress-enhanced chain scission.

**The extent of scission** is an internal variable, defined as a local dimensionless measure $\xi(\mathbf{x}, t)$, which was introduced to model and track the progression of chain scission.(Kannan and Rajagopal, 2011; Loeffel et al., 2013; Konica and Sain, 2020; Hajikhani et al., 2021; Pan and Brassart, 2022; Alkhoury and Chester, 2025), such that

$$0 \leq \xi(\mathbf{x}, t) \leq 1\,, \tag{7}$$

where $\xi(\mathbf{x}, t) = 0$ corresponds to a virgin, intact polymer region, and $\xi(\mathbf{x}, t) > 0$ corresponds to a region of polymer that has undergone scission.

# 4 Continuum framework and constitutive equations

In this section, we provide an overview of the foundational ingredients for developing the continuum-level framework to describe the quasi-static elastic-plastic constitutive behavior of photo-degrading cellulose acetate under isothermal conditions.

## 4.1 Kinematics

Consider an undeformed body $\mathcal{B}_{\mathrm{R}}$ identified with the region of space it occupies in a fixed reference configuration, and denote by $\mathbf{x}_{\mathrm{R}}$ an arbitrary material point of $\mathcal{B}_{\mathrm{R}}$. The referential body $\mathcal{B}_{\mathrm{R}}$ then undergoes a motion $\mathbf{x} = \boldsymbol{\chi}(\mathbf{x}_{\mathrm{R}}, t)$ to the deformed body $\mathcal{B}_t$ with deformation gradient and velocity gradient given by

$$\mathbf{F} = \nabla\boldsymbol{\chi}, \qquad \mathbf{L} = \operatorname{grad}\mathbf{v} = \dot{\mathbf{F}}\mathbf{F}^{-1}\,. \tag{8}$$

changes in entanglement density directly influence the strain-hardening modulus (i.e., the hardening slope in a stress–strain curve).

Further, the polar decomposition of the deformation gradient

$$\mathbf{F} = \mathbf{R}\mathbf{U} = \mathbf{V}\mathbf{R} \tag{9}$$

allows its split into a rotation tensor $\mathbf{R}$, and the symmetric stretch tensors $\mathbf{U}$ and $\mathbf{V}$ as is standard in the literature and defined as

$$\mathbf{U} = \sqrt{\mathbf{F}^{\top}\mathbf{F}}\,, \qquad \mathbf{V} = \sqrt{\mathbf{F}\mathbf{F}^{\top}}\,. \tag{10}$$

Additionally, the right and left Cauchy-Green deformation tensors are given by

$$\mathbf{C} = \mathbf{U}^2 = \mathbf{F}^{\top}\mathbf{F}\,, \qquad \text{and} \qquad \mathbf{B} = \mathbf{V}^2 = \mathbf{F}\mathbf{F}^{\top}\,. \tag{11}$$

In general, since photo-degrading polymers can undergo multiple relaxation and deformation mechanisms, we adopt the multi-mechanism approach to the multiplicative Kröner-Lee decomposition (Kröner, 1959; Lee, 1969), which takes the form

$$\mathbf{F} = \mathbf{F}^{e\,(\alpha)}\mathbf{F}^{p\,(\alpha)}\,, \text{ with } J^{e(\alpha)} = \det \mathbf{F}^{e\,(\alpha)} > 0\,, \text{ and } J^{p(\alpha)} = \det \mathbf{F}^{p\,(\alpha)} > 0\,,\ \alpha = 1, \ldots, M, \tag{12}$$

where the deformation gradient $\mathbf{F}$ is split into an elastic $\mathbf{F}^{e\,(\alpha)}$ and a plastic $\mathbf{F}^{p\,(\alpha)}$, and each $\alpha$ represents a specific micromechanism of deformation (Buckley and Jones, 1995; Bergström and Boyce, 1998; Boyce et al., 2000; Dooling et al., 2002; Dupaix and Boyce, 2007; Anand et al., 2009; Ames et al., 2009; Srivastava et al., 2010; Sain et al., 2018). Starting with (8) and (12), we write the velocity gradient as

$$\mathbf{L} = \dot{\mathbf{F}}\mathbf{F}^{-1} = \mathbf{L}^{e\,(\alpha)} + \mathbf{F}^{e\,(\alpha)}\mathbf{L}^{p\,(\alpha)}\mathbf{F}^{e\,(\alpha)-1} \tag{13}$$

where

$$\mathbf{L}^{e\,(\alpha)} = \dot{\mathbf{F}}^{e\,(\alpha)}\mathbf{F}^{e\,(\alpha)-1}, \qquad \text{and} \qquad \mathbf{L}^{p\,(\alpha)} = \dot{\mathbf{F}}^{p\,(\alpha)}\mathbf{F}^{p\,(\alpha)-1}\,, \tag{14}$$

are the elastic and plastic velocity gradients, respectively. We also introduce the corresponding elastic and plastic stretching and spin tensors such that

$$\begin{aligned} \mathbf{D} &= \operatorname{sym} \mathbf{L}\,, & \mathbf{W} &= \operatorname{skw} \mathbf{L}\,, \\ \mathbf{D}^{e\,(\alpha)} &= \operatorname{sym} \mathbf{L}^{e\,(\alpha)}\,, & \mathbf{W}^{e\,(\alpha)} &= \operatorname{skw} \mathbf{L}^{e\,(\alpha)}\,, \\ \mathbf{D}^{p\,(\alpha)} &= \operatorname{sym} \mathbf{L}^{p\,(\alpha)}\,, & \mathbf{W}^{p\,(\alpha)} &= \operatorname{skw} \mathbf{L}^{p\,(\alpha)}\,, \end{aligned} \tag{15}$$

such that $\mathbf{L} = \mathbf{D} + \mathbf{W}$, $\mathbf{L}^{e\,(\alpha)} = \mathbf{D}^{e\,(\alpha)} + \mathbf{W}^{e\,(\alpha)}$, and $\mathbf{L}^{p\,(\alpha)} = \mathbf{D}^{p\,(\alpha)} + \mathbf{W}^{p\,(\alpha)}$. Further, our interest lies with isotropic materials, for which plastic flow is typically taken to be irrotational such that

$$\mathbf{W}^{p\,(\alpha)} = \mathbf{0}\,. \tag{16}$$

As a consequence, $\mathbf{L}^{p\,(\alpha)} = \mathbf{D}^{p\,(\alpha)}$, and

$$\dot{\mathbf{F}}^{p\,(\alpha)} = \mathbf{D}^{p\,(\alpha)} \mathbf{F}^{p\,(\alpha)}\,. \tag{17}$$

Further, the former relations hold for both elastic and plastic parts, i.e.,

$$\begin{aligned} \mathbf{F}^{e\,(\alpha)} &= \mathbf{R}^{e\,(\alpha)} \mathbf{U}^{e\,(\alpha)} = \mathbf{V}^{e\,(\alpha)} \mathbf{R}^{e\,(\alpha)}\,, \\ \mathbf{U}^{e\,(\alpha)} &= \sqrt{\mathbf{F}^{e\,(\alpha)\top} \mathbf{F}^{e\,(\alpha)}}\,, \quad \mathbf{V}^{e\,(\alpha)} = \sqrt{\mathbf{F}^{e\,(\alpha)} \mathbf{F}^{e\,(\alpha)\top}}\,, \end{aligned} \tag{18}$$

and

$$\mathbf{C}^{e\,(\alpha)} = \mathbf{U}^{e\,(\alpha)2} = \mathbf{F}^{e\,(\alpha)\top} \mathbf{F}^{e\,(\alpha)}\,, \quad \mathbf{B}^{e\,(\alpha)} = \mathbf{V}^{e\,(\alpha)2} = \mathbf{F}^{e\,(\alpha)} \mathbf{F}^{e\,(\alpha)\top}\,, \tag{19}$$

with

$$\begin{aligned} \mathbf{F}^{p\,(\alpha)} &= \mathbf{R}^{p\,(\alpha)} \mathbf{U}^{p\,(\alpha)} = \mathbf{V}^{p\,(\alpha)} \mathbf{R}^{p\,(\alpha)}\,, \\ \mathbf{U}^{p\,(\alpha)} &= \sqrt{\mathbf{F}^{p\,(\alpha)\top} \mathbf{F}^{p\,(\alpha)}}\,, \quad \mathbf{V}^{p\,(\alpha)} = \sqrt{\mathbf{F}^{p\,(\alpha)} \mathbf{F}^{p\,(\alpha)\top}}\,, \end{aligned} \tag{20}$$

and

$$\mathbf{C}^{p\,(\alpha)} = \mathbf{U}^{p\,(\alpha)2} = \mathbf{F}^{p\,(\alpha)\top}\mathbf{F}^{p\,(\alpha)}\,, \quad \mathbf{B}^{p\,(\alpha)} = \mathbf{V}^{p\,(\alpha)2} = \mathbf{F}^{p\,(\alpha)}\mathbf{F}^{p\,(\alpha)\top}\,. \tag{21}$$

## 4.2 Specialization of constitutive equations

In Alkhoury et al. (2024), the uniaxial tensile experiments were performed at a single strain rate ($\dot{\varepsilon} = 10^{-3}$ s$^{-1}$). Given this limited data, we focus our attention here on a single micromechanism ($\alpha = 1$) to capture the mechanical response of pre-exposed materials. Consequently, (12) and (17) can be recast

$$\mathbf{F}^{(1)} = \mathbf{F} = \mathbf{F}^e\mathbf{F}^p\,, \qquad \text{with} \qquad \det\mathbf{F}^e > 0 \qquad \text{and} \qquad \det\mathbf{F}^p > 0\,, \tag{22}$$

and

$$\dot{\mathbf{F}}^{p(1)} = \dot{\mathbf{F}}^p = \mathbf{D}^p\mathbf{F}^p\,. \tag{23}$$

Lastly, plastic flow is assumed to be incompressible such that

$$J^p = 1, \tag{24}$$

and as a result

$$\operatorname{tr}\mathbf{L}^p = \operatorname{tr}\mathbf{D}^p = 0\,, \tag{25}$$

and therefore

$$J^e = J\,. \tag{26}$$

### 4.2.1 Free energy and stress

Since photo-degrading cellulose acetate subjected to concurrent stresses shows a typical elastic-plastic behavior with linear strain hardening, we start by laying the general foundations of our constitutive framework, based on rate-dependent plasticity with linear hardening (Gurtin et al., 2010).

We take a free energy per unit intermediate volume in the form

$$\psi^e = G|\mathbf{E}_0{}^e|^2 + \frac{1}{2}K(\operatorname{tr}\mathbf{E}^e)^2\,, \tag{27}$$

where $G$ and $K$ are the shear and bulk moduli, respectively, and are taken to be constants following the results from Figure 8a that show the elastic modulus was unaffected by UV exposure. $\mathbf{E}_0^e$ is the deviatoric part of the logarithmic elastic strain $\mathbf{E}^e = \ln \mathbf{U}^e$. Next, the corresponding Mandel stress is obtained

$$\mathbf{M}^e = \frac{\partial \hat{\psi}^e}{\partial \mathbf{E}^e} = 2G\mathbf{E}_0^e + K(\operatorname{tr}\mathbf{E}^e)\mathbf{1}\,, \tag{28}$$

which is work conjugate to $\mathbf{D}^p$. Since the material is isotropic, the Cauchy stress is related to Mandel stress by

$$\mathbf{T} = J^{-1}\mathbf{R}^e\mathbf{M}^e\mathbf{R}^{e\top}\,. \tag{29}$$

### 4.2.2 Plastic flow

Now, keeping (22) and (23) in mind, we write the flow rule in the equivalent tensile representation

$$\mathbf{D}^p = \sqrt{\frac{3}{2}}\dot{\epsilon}^p\mathbf{N}^p\,, \tag{30}$$

where $\dot{\epsilon}^p$ and $\mathbf{N}^p$ are the equivalent tensile plastic strain rate and the direction of plastic flow, respectively. Moreover, the strength relation is given by

$$\bar{\sigma} = S\,, \tag{31}$$

where

$$\bar{\sigma} \overset{\text{def}}{=} \sqrt{\frac{3}{2}\mathbf{M}_0^e : \mathbf{M}_0^e}\,, \tag{32}$$

is the equivalent tensile stress. The direction of plastic flow is taken as

$$\mathbf{N}^p = \sqrt{\frac{3}{2}}\frac{\mathbf{M}_0^e}{\bar{\sigma}}\,, \tag{33}$$

where $\mathbf{M}_0^e$ is the deviator of the Mandel stress. Lastly, the equivalent accumulated plastic is given by

$$\bar{\epsilon}^p \stackrel{\text{def}}{=} \int_0^t \dot{\bar{\epsilon}}^p(\zeta)d\zeta\,. \tag{34}$$

### 4.2.3 Extent of scission

To account for chain scission due to photo-degradation, we specialize the extent of scission such that

$$\hat{\xi}(\mathbb{D},\bar{\sigma}) \stackrel{\text{def}}{=} \frac{T_{g0} - \hat{T}_g(\mathbb{D},\bar{\sigma})}{T_{g0} - T_{g,min}}\,, \tag{35}$$

where $T_{g0}$, $\hat{T}_g(\mathbb{D},\bar{\sigma})$, and $T_{g,min}$ correspond to the initial glass transition temperature for a virgin material, the current glass transition temperature for a UV dose and applied stress, and the minimum glass transition temperature, respectively. We note that although a common definition of the extent of scission is based on the molecular weight $\xi \stackrel{\text{def}}{=} 1 - \frac{M_{\text{n}}}{M_{\text{n}_0}}$, we use $T_g$ as a surrogate measure of chain scission following the Flory-Fox relation (Fox Jr and Flory, 1950) since those measurements are more common and simpler.

Moreover, since $T_g$ decreases with UV exposure, and even further decreases under an applied stress as shown in Figure 5, we use a constitutive equation for the glass transition temperature in the form

$$\dot{T}_g = -k_{sc}(\bar{\sigma})I\,, \quad T_g\left(\mathbf{x}_{\text{R}}, t=0\right) = T_{g0}\,, \tag{36}$$

where $k_{sc}$ is a stress-dependent reaction rate constant[4] for the chain scission mechanism, and $I$ is the local light intensity. The stress-dependent reaction rate is constitutively prescribed

[4]In general, the rate of chemical reactions is affected by the absorptivity of the material (cf. eg., Long et al., 2009), but is neglected here due to the lack of experimental data.

such that

$$k_{sc} = k_v + k_s \bar{\sigma}\,, \tag{37}$$

where $k_v$ represents the baseline reaction rate for a virgin material and $k_s$ is a material parameter that controls its stress-dependent rate of change. This constitutive choice was made since a decrease in $T_g$ is only expected to occur upon UV exposure (i.e., $\xi$ can only evolve when $I \neq 0$), and it is known that the stress affects the rate of reaction in polymeric materials (Silberstein et al., 2013; Kim et al., 2015; Vidavsky et al., 2019). This includes degradation processes, where mechanical loading can accelerate the rate of degradation (cf. eg., Chen et al., 2025, and references within). Moreover, $\bar{\sigma}$ was adopted as the relevant stress measure in (35) and (37) because the experiments were purely tensile. While the stress measure used to drive reactions may include pressure or triaxiality, we have limited data at this time and thus have assumed the equivalent tensile stress, as it was directly applied in the experiments.

### 4.2.4 Strength evolution

We decompose the total strength $S$ into

$$\hat{S}(\xi, \bar{\sigma}, \bar{\epsilon}^p, \dot{\bar{\epsilon}}^p) = \hat{S}^{\mathrm{SC}}(\xi) + \hat{S}^{\mathrm{RO}}(\xi, \bar{\sigma}) + \hat{S}^{\mathrm{RD}}(\xi, \bar{\epsilon}^p, \dot{\bar{\epsilon}}^p)\,. \tag{38}$$

Such a treatment conveniently identifies the strength components, and allows capturing individual physical mechanisms observed experimentally, as described in Section 3. Starting with the first contribution, $\hat{S}^{\mathrm{SC}}(\xi)$ represents the change in strength due to chain scission alone and is specifically introduced to model traction-free degradation and could be directly measured from the stress-strain curves. Moreover, in the presence of applied stresses and UV exposure, $\hat{S}^{\mathrm{RO}}(\xi, \bar{\sigma})$ is introduced to model the increase in yield due to chain reorientation. Moving onto the rate-dependent contribution, and since the experimental results are reasonably captured by a simple linear hardening model upon plastic deformation, $\hat{S}^{\mathrm{RD}}(\xi, \bar{\epsilon}^p, \dot{\bar{\epsilon}}^p)$ is

chosen accordingly.

First, the reaction-dependent strength for traction-free degradation decreases with chain scission. Consequently, we specialize its evolution such that

$$\dot{S}^{\mathrm{SC}}(\xi) = -R_{sc}\dot{\xi}\,, \quad S^{\mathrm{SC}}\left(\mathbf{x}_{\mathrm{R}}, t=0\right) = S_0^{\mathrm{SC}}\,, \tag{39}$$

where $R_{sc} > 0$ and $S_0^{\mathrm{SC}} > 0$ are material parameters that correspond to the rate of evolution and the initial yield strength for virgin materials, respectively. This form is chosen since as scission occurs, the decrease in $T_g$ leads the extent of scission from its virgin state (i.e., $\xi = 0$) towards a more degraded state, causing $\hat{S}^{\mathrm{SC}}$ to decrease.

For the opposing contribution due to chain reorientation, we specialize its evolution such that

$$\dot{S}^{\mathrm{RO}}(\xi, \bar{\sigma}) = R_{ro}\mathcal{H}(\bar{\sigma} - \bar{\sigma}_{th})\dot{\xi}\,, \quad S^{\mathrm{RO}}\left(\mathbf{x}_{\mathrm{R}}, t=0\right) = S_0^{\mathrm{RO}}\,, \tag{40}$$

where $R_{ro} > 0$ corresponds to the rate of evolution, $\mathcal{H}$ to the Heaviside function such that

$$\mathcal{H}(\bar{\sigma} - \bar{\sigma}_{th}) = \begin{cases} 1 & \text{if } \bar{\sigma} \geq \bar{\sigma}_{th} \\ \\ 0 & \text{if } \bar{\sigma} < \bar{\sigma}_{th}\,, \end{cases} \tag{41}$$

where $\bar{\sigma}_{th}$ represents an applied stress threshold, and $S_0^{\mathrm{RO}} \geq 0$ an initial yield strength. This form is chosen since the increased energy due to UV allows for strain hardening due to chain reorientation only after exceeding a stress threshold distinct from the yield, resulting in an increased yield.[5]

Lastly, the strength due to plastic flow can be described by a rate-dependent flow rule with hardening such that

$$S^{\mathrm{RD}}(\xi, \bar{\epsilon}^p, \dot{\bar{\epsilon}}^p) = \hat{H}(\xi)\bar{\epsilon}^p \left(\frac{\dot{\bar{\epsilon}}^p}{\dot{\epsilon}_0}\right)^m\,, \tag{42}$$

where we specialize $\hat{H}(\xi)$. Based on the experimental results, the reaction-dependent hard-

[5]We note here that while (39) and (40) can be combined, experimental results indicate that each reaction-dependent mechanism progresses at a distinct rate and, therefore, needs not to be combined.

ening slope decreases with chain scission for all applied stresses. Consequently, we specialize $\hat{H}(\xi)$ such that

$$H(\xi) = H_v - H_b\xi\,, \tag{43}$$

where $H_v$ represents the baseline hardening slope for a virgin material and $H_b$ is a material parameter that controls its rate of change.

## 4.3 Governing equations

In this section, we overview the governing continuum-level equations to describe the mechanical behavior of photo-degrading cellulose acetate subjected to stress.

### 4.3.1 Balance of forces and moments

As is standard, neglecting inertial effects, the balance of forces and moments in the deformed body $\mathcal{B}_t$ are expressed as

$$\mathrm{div}\mathbf{T} + \mathbf{b} = \mathbf{0} \quad \text{and} \quad \mathbf{T} = \mathbf{T}^\top, \tag{44}$$

where $\mathbf{b}$ is the body force.

### 4.3.2 Radiative transfer

Building upon existing literature and our recent work (Modest and Mazumder, 2021; Alkhoury and Chester, 2025), the governing equation for radiative transfer, for each frequency $\nu$, can be expressed as

$$\frac{1}{c}\frac{\partial I^{(\nu)}}{\partial t} + \mathbf{s}\cdot\mathrm{grad}\, I^{(\nu)} = j_\nu - k_\nu I^{(\nu)} - k_{s\nu} I^{(\nu)} + \frac{k_{s\nu}}{4\pi}\int_{4\pi} I^{(\nu)}\Phi_\nu d\omega\,, \quad \forall\,\nu\,, \tag{45}$$

where $c$ is the speed of light, $I^{(\nu)}$ is the spectral radiative intensity, $j_\nu$ is the emission coefficient, $k_\nu$ is the absorption coefficient, $k_{s\nu}$ is the scattering coefficient, and $\Phi_\nu$ is the scattering phase function. Equation (45) indicates that as a beam of light travels through a

participating medium along a known path $\mathbf{s}$, its intensity is decreased by absorption $k_\nu I^{(\nu)}$ and scattering away $k_{s\nu} I^{(\nu)}$ (out-scattering), and augmented by emission $j_\nu$ and scattering from other directions into the direction of travel (in-scattering), as shown in the last integral term. In most engineering applications, the appropriate time scale is significantly longer than the transmission time through the body. Moreover, neglecting scattering and emission, and assuming monochromatic light, (45) can be recast in the form

$$\mathbf{s} \cdot \operatorname{grad} I + \beta I = 0\,, \tag{46}$$

where $\mathbf{s}$ is the local direction in which light is propagating, and $\beta(\mathbf{x}, t)$ is the extinction field that takes into account the attenuation of the light inside the material.

# 5 Calibration

In this section, we describe the calibration process using both micro- and macro-scale experimental results. The micro-scale results are used to inform the model about the material's degraded state by relating the extent of scission to the glass transition temperature. The macro-scale results are used to inform the model about the broader constitutive response.

First, we numerically implement (36) and use the results from Figure 5 to calibrate for $k_v$ and $k_s$, and $T_{g0}$, as shown in Figure 9a with material parameters reported in Table 2. We note and remind the reader that the light intensity was approximated by an experimentally measured quasi-uniform "average intensity," that corresponds to $\bar{I} = 34.316$ W/m$^2$. Next, we use (35) to calculate the extent of scission $\xi$, as shown in Figure 9b with $T_{g,min}$ reported in Table 2. Lastly, using this information, we obtain the relationship between $\xi$ and UV dose shown in Figure 9c and use it in what follows.

Moving onto the constitutive response, we use the results from Figures 8b and 9c to plot the reaction-dependent contribution to the strength, $S^{\mathrm{SC}}$, due to chain scission, for the traction-free case in terms of $\xi$. We then calibrate it using (39) as can be observed

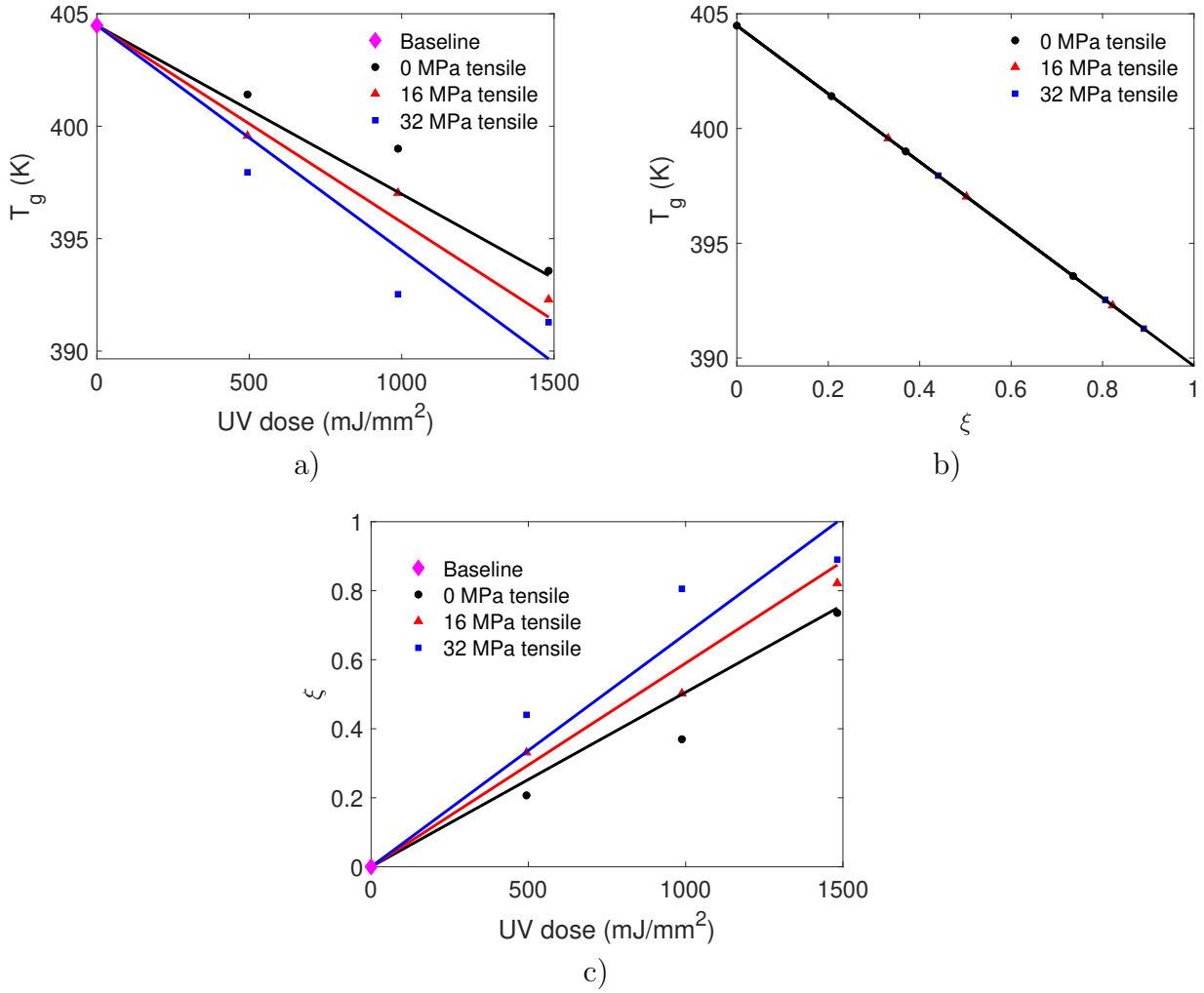


Figure 9: a) Calibration of $T_g$ evolution for different UV doses, b) the relationship between $T_g$ and $\xi$ using (35), and c) the relationship between $\xi$ and UV doses for photo-degrading cellulose acetate, at different applied stress. Note that the model fit is represented using solid lines.

in Figure 10a, and the material parameters are reported in Table 2. Moreover, we plot the difference in yield strength between the traction-free (labeled $S_0$ in the plot) and the degradation under 32 MPa tensile (labeled $S_{32}$ in the plot), and use it to calibrate for the opposing contribution, $S^{\mathrm{RO}}$, due to chain reorientation induced strain hardening using (40) as can be observed in Figure 10b, with material parameters reported in Table 2. We note that there was no significant increase in yield for an applied stress of 16 MPa tensile; for that reason, the stress threshold $\bar{\sigma}_{th}$ is taken to be 32 MPa due to a lack of more comprehensive

| | |
|---|---|
| $E$ (GPa) | 3.2 |
| $\nu^{\text{poi}}$ | 0.47 |
| $T_{g0}$ (K) | 404.48 |
| $T_{g,min}$ (K) | 389.65 |
| $k_v$ (K m$^2$/J) | 7.5 $\times 10^{-6}$ |
| $k_b$ (K m$^2$/J Pa) | 7.8125 $\times 10^{-14}$ |
| $S_0^{\text{SC}}$ (MPa) | 59.96 |
| $R_{sc}$ (MPa) | 15.45 |
| $S_0^{\text{RO}}$ (MPa) | 0 |
| $R_{ro}$ (MPa) | 15.18 |
| $\bar{\sigma}_{th}$ (MPa) | 32 |
| $H_v$ (MPa) | 199.29 |
| $H_b$ (MPa) | 108.9 |
| $\dot{\varepsilon}_0$ (1/s) | $10^{-3}$ |
| $m$ | 0.01 |
| $\beta$ (1/m) | 7000 |

Table 2: Calibrated material parameters for photo-degrading cellulose acetate.

data. We also note that while the model can predict $\hat{S}^{\text{SC}}(\xi)$ and $\hat{S}^{\text{RO}}(\xi, \bar{\sigma})$ for a range of conditions, one should not attempt to extrapolate the reaction-dependent threshold strength predictions beyond the calibrated range as sample failure is very likely as observed in the experiments.

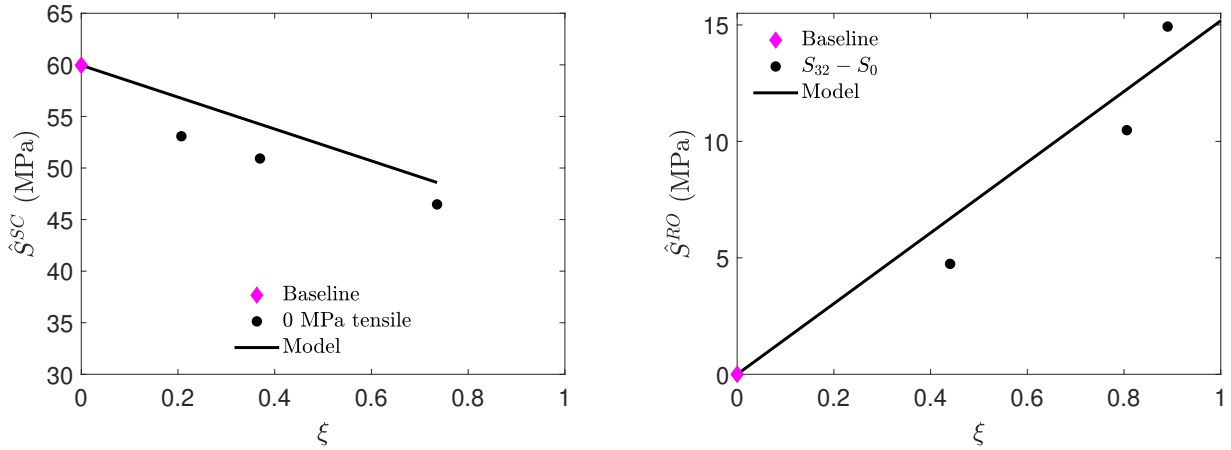


Figure 10: Calibration of the strength evolution due to pre-exposure a) $\hat{S}^{\text{SC}}(\xi)$ for traction-free photo-degrading cellulose acetate, and b) $\hat{S}^{\text{RO}}(\xi, \bar{\sigma})$ for photo-degrading cellulose acetate at an applied stress.

Next, we use the results from Figures 9c and 8d to plot the reaction-dependent hardening slope $\hat{H}(\xi)$ in terms of $\xi$, for different applied stresses. Likewise, we calibrate for the reaction-dependent hardening slope using (43) as can be observed in Figure 11, and the material parameters are reported in Table 2. We also note that while the model can predict $\hat{H}(\xi)$ for a range of conditions, one should not attempt to predict beyond the calibrated range as material failure is very likely.

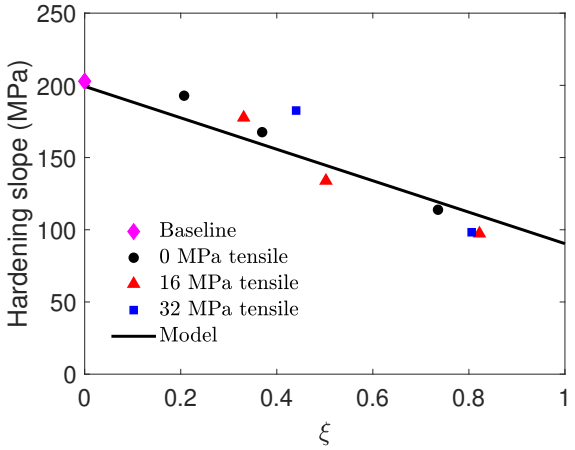


Figure 11: Calibration of the reaction-dependent hardening slope $\hat{H}(\xi)$ for photo-degrading cellulose acetate at different applied stresses.

Lastly, we assume incompressibility and implement a 1D version of the constitutive model introduced in Section 4.2 using the calibrated material parameters from Table 2 to obtain the full constitutive response of previously photo-degraded cellulose acetate as can be seen in Figure 12, where we can see a good agreement between our model and the uniaxial experimental results.

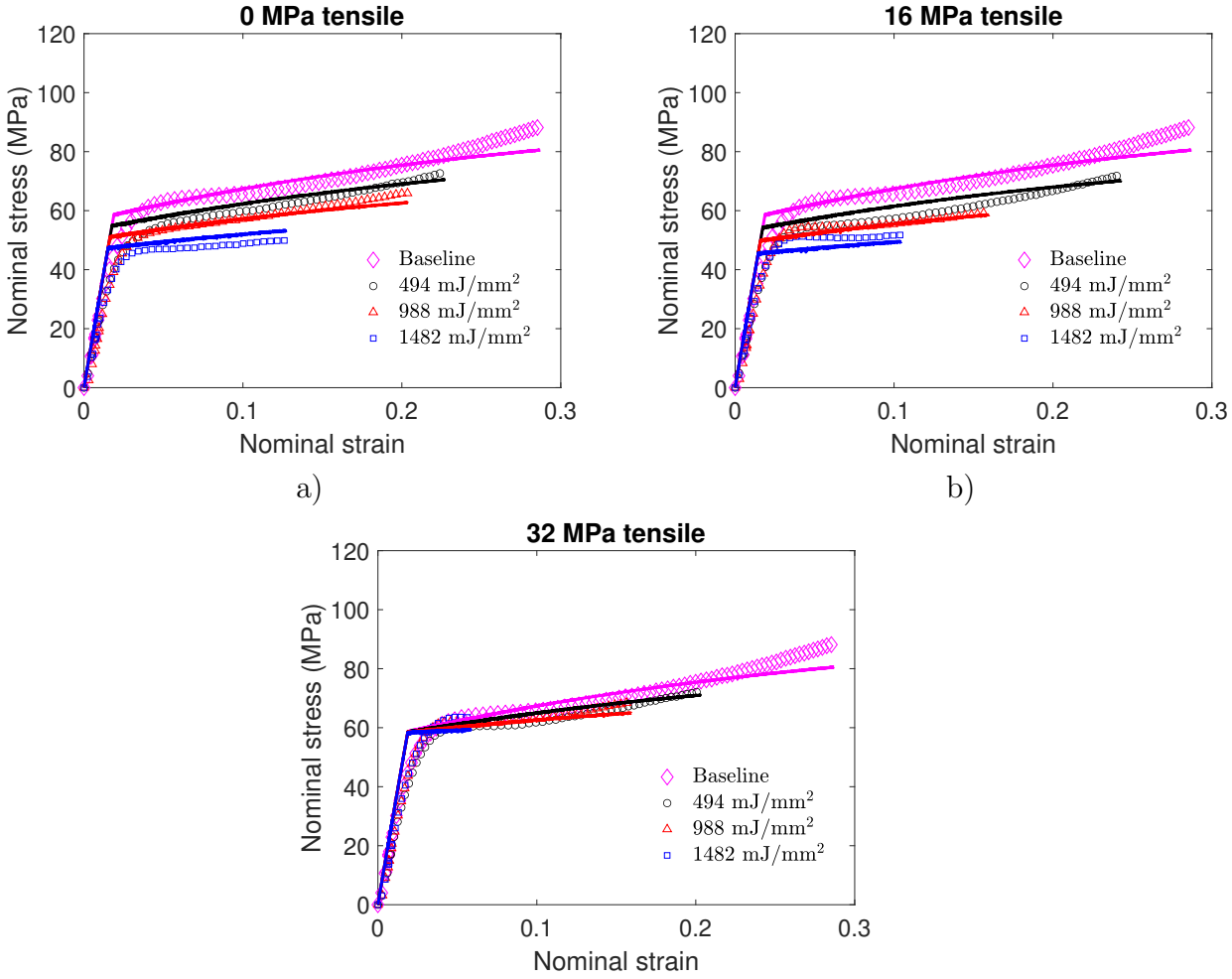


Figure 12: Constitutive model calibration of photo-degrading cellulose acetate for different UV doses for a) traction-free degradation, b) degradation at an applied stress of 16 MPa tensile, and c) 32 MPa tensile. Note that the model fit is represented using solid lines.

# 6 Application of the model

In this section, building on our previous work (Chester et al., 2015; Hamel et al., 2017; Alkhoury and Chester, 2025), we implement our model as a user-defined element (UEL) subroutine in the commercial finite element software package ABAQUS (Abaqus/Standard, 2024). We then use it to revisit our benchmark problem (Alkhoury and Chester, 2025), in which we consider three-dimensional photo-degradation under stress to demonstrate the effect of stress-enhanced photo-degradation in cellulose acetate used in this work.

Specifically, we consider two geometries as shown in Figure 13, (i) a rectangular plate (Figure 13a), and (ii) a notched rectangular plate (Figure 13b). The overall dimensions are $L_0 = 1\,\text{mm}$, $W_0 = 1\,\text{mm}$, $t_0 = 0.1\,\text{mm}$. The notched rectangular plate has a notch radius of $R = 0.05\,\text{mm}$ at the center along the top face. The simulation consists of two steps. In the first step, the material is mechanically loaded by applying a traction $\sigma_\infty = 12\,\text{MPa}$ over $10\,\text{s}$. In the second step, the applied traction remains fixed, and the material's top surface is exposed to light irradiation at an incident intensity $I_0 = 250\,\text{W/m}^2$ for $1\,\text{hour}$. With one geometry featuring a notch, the stress concentration enables the coupling between mechanics and degradation to be easily observed when compared to the un-notched plate.

The boundary conditions are shown in Figure 13, and described as follows.

- The top face: An incident light irradiation, $I = I_0$, is applied at the top face, which is traction-free.
- The bottom face: A roller boundary condition is applied to the bottom face such that $u_2 = 0$.
- The lateral faces: A tensile traction of $\sigma_\infty$ is applied to the lateral surfaces.
- The front and back faces: The front and back faces are traction-free.

Due to the symmetry, we only simulate one quarter of the geometry. Specifically, the mesh consists of 1200 8-node linear user elements with one element through the (half-)thickness

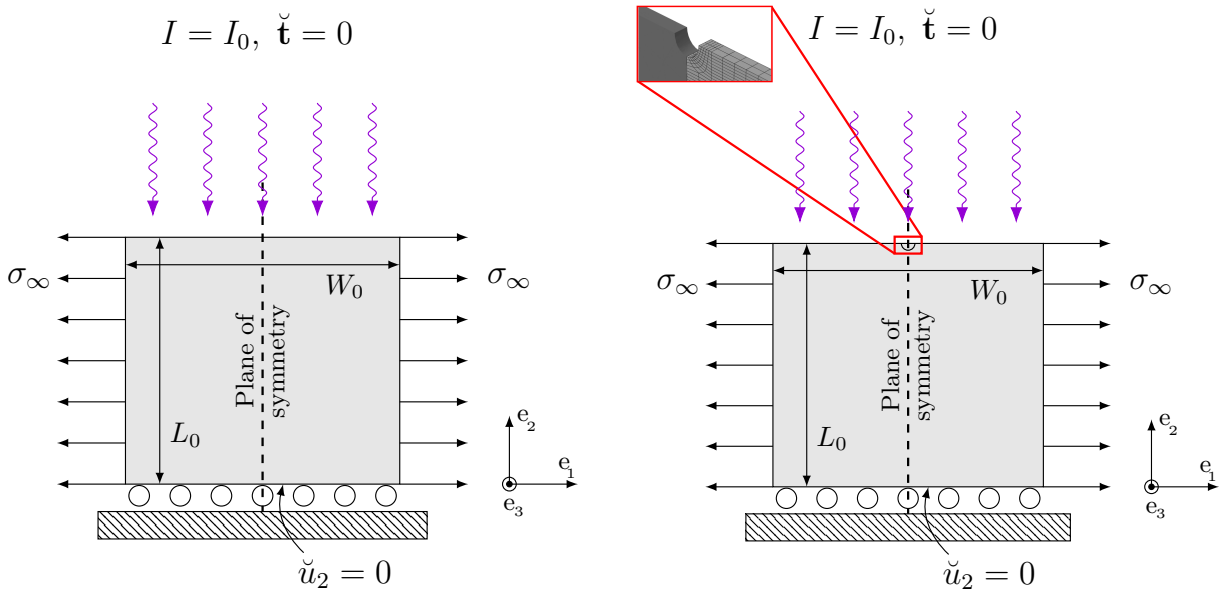


a) b)

Figure 13: Schematic showing the geometry and boundary conditions illustrating the three-dimensional photo-degradation to a unidirectional monochromatic light for the a) rectangular plate, and b) the notched rectangular plate.

for the rectangular plate, and 2708 8-node linear user elements with two elements through the (half-)thickness for the notched rectangular plate.

Figure 14 shows the simulation results after 1 hour of irradiation. For easy comparison, the two geometries are shown side by side: un-notched on the left and notched on the right. Starting with Figure 14a, it can be observed that for the un-notched body, there is no stress concentration and everywhere $\bar{\sigma} = \sigma_\infty$. On the other hand, for the notched body, the maximum stress concentration at the notch tip is roughly $\bar{\sigma} \approx 3\sigma_\infty$.

Next, as light travels through both geometries, its intensity attenuates, as can be observed in Figure 14b. This result is expected, the intensity attenuates as the light travels through the body.

As shown in Figure 14c, after 1 hour of light exposure, the extent of degradation, denoted

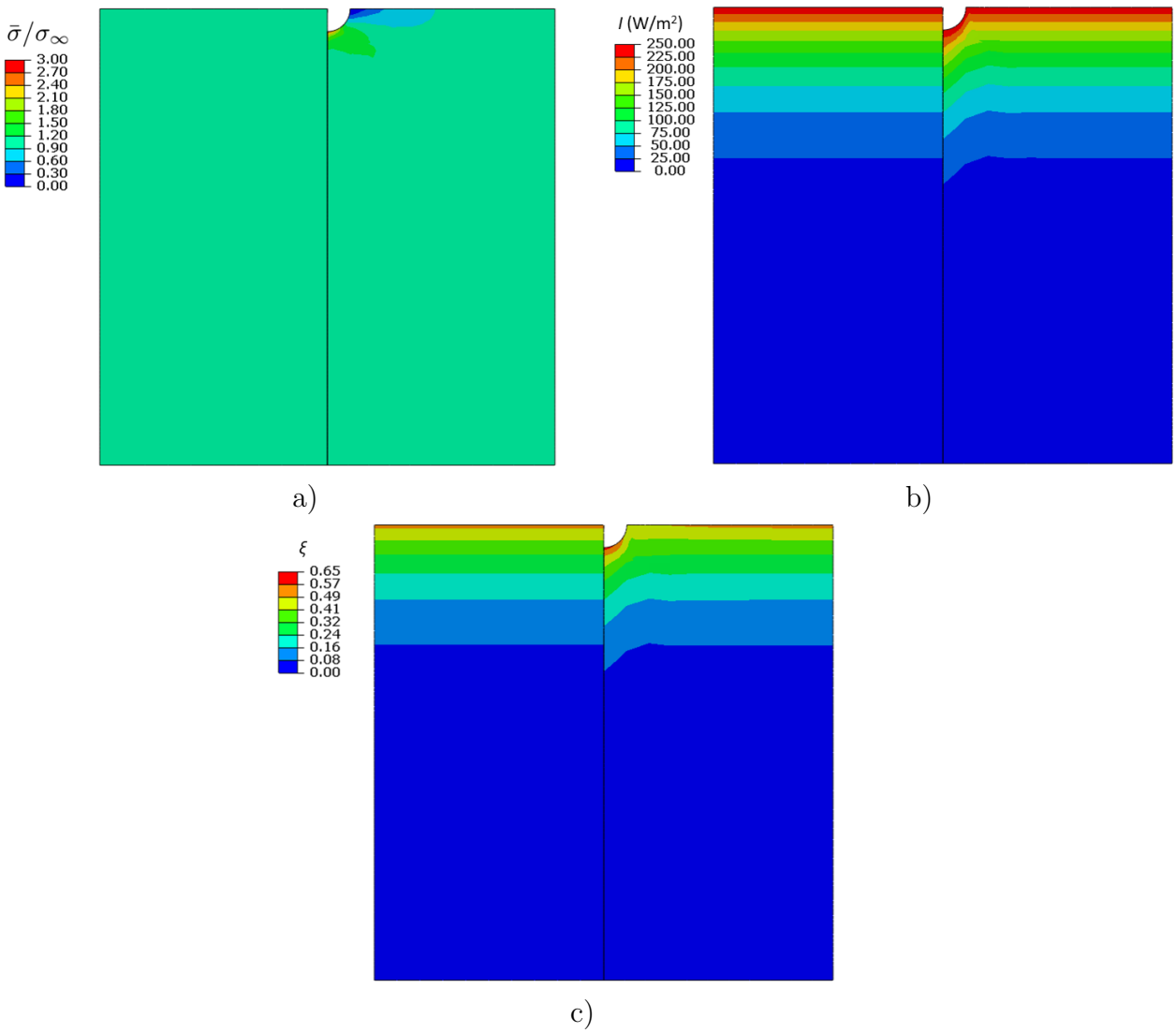


Figure 14: Contour plots of the: a) stress concentration factor, b) light intensity, and c) extent of degradation for the degradation after 1 hour of irradiation. We note that the left half of each image corresponds to the un-notched case, while the right half corresponds to the notched case, side by side for easy comparison.

by $\xi$, clearly shows how the stress impacts the degradation. For the un-notched body, $\xi$ exhibits a non-uniform distribution where $\xi$ is highest ($\xi \approx 0.49$) near the top surface, which is expected since the light intensity is highest near this region. For the notched body, $\xi$ remains highest near the top surface; however, it is more pronounced near the notch ($\xi \approx 0.63$), which can be attributed to the stress-enhanced photo-degradation.

# 7 Conclusion

In this work, we have built upon our recent contribution (Alkhoury et al., 2024) and developed a continuum-level constitutive model for photo-degrading cellulose acetate subjected to concurrent stress. The model was built on rate-dependent plasticity and informed by both microstructural and macro-scale information. The novelty of this work lies in the combined use of multi-scale information with stress coupling into the overall constitutive response.

The experimental results reported in Alkhoury et al. (2024) suggested that upon photo-degradation, the material undergoes microstructural changes due to UV irradiation, which may be further affected by the applied stress. There was no significant change in the Young's modulus, accordingly, our model assumed a constant Young's modulus. The yield strength showed a unique transitional behavior: decreasing as the UV dose increase, and increasing after a stress threshold while the UV dose increase. Consequently, our model included a dependence of the yield strength on two competing mechanisms affected by chain scission and strain hardening due to chain reorientation, due to the applied stresses in the presence of UV. The hardening slope exhibited a decreasing trend with UV exposure and stress application. Consequently, our model included a dependence of the hardening slope on the stress-enhanced chain scission. Lastly, the model was calibrated against the micro- and macro- scale experiments reported in Alkhoury et al. (2024).

The outcome of this work enables the prediction of the mechanical behavior of photo-degrading amorphous polymers while subjected to stresses. This can help engineers design and use devices made from renewable and degradable materials without sacrificing the devices' performance or integrity.

Our future research will focus on additional experiments to inform our subsequent modeling work. In experimental endeavors, it remains crucial to investigate rate-dependent phenomena, such as strain-rate dependence and strains arising from creep-like permanent deformation, including chain sliding and reorientation, under stress below the yield point. Motivated by these experimental findings, we will further expand our model to account for

this behavior, thus enhancing its capabilities.

## CRediT authorship contribution statement

**Keven Alkhoury**: Conceptualization, Investigation, Writing - Original Draft. **Laurence Brassart**: Writing - Review & Editing. **Shawn A. Chester**: Conceptualization, Supervision, Writing - Review & Editing, Funding acquisition.

## Acknowledgments

KA acknowledges partial support from the Hibbitt Engineering Fellowship at Brown University. SAC acknowledges partial support from the National Science Foundation, USA under grant number (CMMI-1751520). LB acknowledges support from UK Research and Innovation through a Future Leaders Fellowship ([MR/W006995/1]). The opinions, findings, and conclusions, or recommendations expressed are those of the author(s) and do not necessarily reflect the views of the National Science Foundation. The authors gratefully acknowledge Nicholas S. Elmasri and Mark Nyevgen for assistance with data verification.

# References


Abaqus/Standard. *Abaqus Reference Manuals*. Dassaults Systemes Simulia, Johnston, RI, 2024.

K. Alkhoury and S. A. Chester. A chemo-thermo-mechanically coupled theory of photo-reacting polymers: Application to modeling photo-degradation with irradiation-driven heat transfer. *Journal of the Mechanics and Physics of Solids*, page 106050, 2025.

K. Alkhoury, C. Zhang, G. Liu, K. McEnnis, L. Brassart, S. Nadimpalli, and S. A. Chester. Investigating the influence of stress on uv-induced degradation in cellulose acetate: A comprehensive experimental characterization. *International Journal of Solids and Structures*, page 113086, 2024.

N. M. Ames, V. Srivastava, S. A. Chester, and L. Anand. A thermo-mechanically coupled theory for large deformations of amorphous polymers. part ii: Applications. *International Journal of Plasticity*, 25(8):1495–1539, 2009.

L. Anand, N. M. Ames, V. Srivastava, and S. A. Chester. A thermo-mechanically coupled theory for large deformations of amorphous polymers. part i: Formulation. *International Journal of Plasticity*, 25(8):1474–1494, 2009.

M. Asgher, S. A. Qamar, M. Bilal, and H. M. Iqbal. Bio-based active food packaging materials: Sustainable alternative to conventional petrochemical-based packaging materials. *Food Research International*, 137:109625, 2020.

G. Ayoub, A. Rodriguez, B. Mansoor, and X. Colin. Modeling the visco-hyperelastic–viscoplastic behavior of photodegraded semi-crystalline low-density polyethylene films. *International Journal of Solids and Structures*, 204:187–198, 2020.

A. Bahrololoumi, V. Morovati, E. A. Poshtan, and R. Dargazany. A multi-physics con-

stitutive model to predict hydrolytic aging in quasi-static behaviour of thin cross-linked polymers. *International Journal of Plasticity*, 130:102676, 2020.

A. Bahrololoumi, V. Morovati, M. Shaafaey, and R. Dargazany. A multi-physics approach on modeling of hygrothermal aging and its effects on constitutive behavior of cross-linked polymers. *Journal of the Mechanics and Physics of Solids*, 156:104614, 2021.

A. Bahrololoumi, M. Shaafaey, G. Ayoub, and R. Dargazany. Thermal aging coupled with cyclic fatigue in cross-linked polymers: Constitutive modeling & fe implementation. *International Journal of Solids and Structures*, 252:111800, 2022.

S. Belbachir, F. Zaïri, G. Ayoub, U. Maschke, M. Naït-Abdelaziz, J.-M. Gloaguen, M. Benguediab, and J.-M. Lefebvre. Modelling of photodegradation effect on elastic–viscoplastic behaviour of amorphous polylactic acid films. *Journal of the Mechanics and Physics of Solids*, 58(2):241–255, 2010.

J. S. Bergström and M. Boyce. Constitutive modeling of the large strain time-dependent behavior of elastomers. *Journal of the Mechanics and Physics of Solids*, 46(5):931–954, 1998.

M. Boyce, S. Socrate, and P. Llana. Constitutive model for the finite deformation stress–strain behavior of poly (ethylene terephthalate) above the glass transition. *Polymer*, 41 (6):2183–2201, 2000.

C. Buckley and D. Jones. Glass-rubber constitutive model for amorphous polymers near the glass transition. *Polymer*, 36(17):3301–3312, 1995.

I. R. Campbell, M.-Y. Lin, H. Iyer, M. Parker, J. L. Fredricks, K. Liao, A. M. Jimenez, P. Grandgeorge, and E. Roumeli. Progress in sustainable polymers from biological matter. *Annual Review of Materials Research*, 53:81–104, 2023.

H. Chen, Z. Pan, G. S. Sulley, C. K. Williams, and L. Brassart. Hydrolytic degradation of amorphous pla: Effect of mechanical loads. *Polymer Degradation and Stability*, page 111751, 2025.

S. A. Chester, C. V. Di Leo, and L. Anand. A finite element implementation of a coupled diffusion-deformation theory for elastomeric gels. *International Journal of Solids and Structures*, 52:1–18, 2015.

P. Dooling, C. Buckley, S. Rostami, and N. Zahlan. Hot-drawing of poly (methyl methacrylate) and simulation using a glass–rubber constitutive model. *Polymer*, 43(8):2451–2465, 2002.

R. B. Dupaix and M. C. Boyce. Constitutive modeling of the finite strain behavior of amorphous polymers in and above the glass transition. *Mechanics of Materials*, 39(1): 39–52, 2007.

A. Eerhart, A. Faaij, and M. Patel. Replacing fossil based pet with biobased pef; process analysis, energy and ghg balance. *Energy & environmental science*, 5(4):6407–6422, 2012.

M. A. Elsawy, K.-H. Kim, J.-W. Park, and A. Deep. Hydrolytic degradation of polylactic acid (pla) and its composites. *Renewable and Sustainable Energy Reviews*, 79:1346–1352, 2017. ISSN 1364-0321. doi: https://doi.org/10.1016/j.rser.2017.05.143. URL `https://www.sciencedirect.com/science/article/pii/S1364032117307876`.

J. Engqvist, M. Wallin, S. A. Hall, M. Ristinmaa, and T. S. Plivelic. Measurement of multi-scale deformation of polycarbonate using x-ray scattering with in-situ loading and digital image correlation. *Polymer*, 82:190–197, 2016.

T. G. Fox Jr and P. J. Flory. Second-order transition temperatures and related properties of polystyrene. i. influence of molecular weight. *Journal of Applied Physics*, 21(6):581–591, 1950.

M. Gardette, A. Perthue, J.-L. Gardette, T. Janecska, E. Földes, B. Pukánszky, and S. Therias. Photo- and thermal-oxidation of polyethylene: Comparison of mechanisms and influence of unsaturation content. *Polymer Degradation and Stability*, 98(11):2383–2390, 2013. ISSN 0141-3910. doi: https://doi.org/10.1016/j.polymdegradstab.2013.07.017. URL `https://www.sciencedirect.com/science/article/pii/S0141391013002395`.

M. Gigliotti, L. Olivier, D. Q. Vu, J.-C. Grandidier, and M. C. Lafarie-Frenot. Local shrinkage and stress induced by thermo-oxidation in composite materials at high temperatures. *Journal of the Mechanics and Physics of Solids*, 59(3):696–712, 2011.

M. E. Gurtin, E. Fried, and L. Anand. *The mechanics and thermodynamics of continua*. Cambridge University Press, 2010.

A. Hajikhani, P. Wriggers, and M. Marino. Chemo-mechanical modelling of swelling and crosslinking reaction kinetics in alginate hydrogels: A novel theory and its numerical implementation. *Journal of the Mechanics and Physics of Solids*, 153:104476, 2021.

C. M. Hamel, F. Cui, and S. A. Chester. A finite element method for light activated shape-memory polymers. *International Journal for Numerical Methods in Engineering*, 111(5): 447–473, 2017.

G. Hayes, M. Laurel, D. MacKinnon, T. Zhao, H. A. Houck, and C. R. Becer. Polymers without petrochemicals: sustainable routes to conventional monomers. *Chemical Reviews*, 123(5):2609–2734, 2022.

E. Hecht. *Optics*. Pearson Education Inc., 2002.

R. S. Hoy and M. O. Robbins. Strain hardening of polymer glasses: Effect of entanglement density, temperature, and rate. *Journal of Polymer Science Part B: Polymer Physics*, 44 (24):3487–3500, 2006.

K. Kannan and K. Rajagopal. A thermodynamical framework for chemically reacting systems. *Zeitschrift für angewandte Mathematik und Physik*, 62(2):331–363, 2011.

J. W. Kim, Y. Jung, G. W. Coates, and M. N. Silberstein. Mechanoactivation of spiropyran covalently linked pmma: effect of temperature, strain rate, and deformation mode. *Macromolecules*, 48(5):1335–1342, 2015.

S. Konica and T. Sain. A thermodynamically consistent chemo-mechanically coupled large deformation model for polymer oxidation. *Journal of the Mechanics and Physics of Solids*, 137:103858, 2020.

S. Konica and T. Sain. A homogenized large deformation constitutive model for high temperature oxidation in fiber-reinforced polymer composites. *Mechanics of Materials*, 160: 103994, 2021.

E. Kröner. Allgemeine kontinuumstheorie der versetzungen und eigenspannungen. *Archive for Rational Mechanics and Analysis*, 4(1):273–334, 1959.

J. H. Lambert. *Photometria sive de mensura et gradibus luminis, colorum et umbrae*. sumptibus vidvae E. Klett, typis CP Detleffsen, 1760.

H. Lamnii, M. N. Abdelaziz, G. Ayoub, X. Colin, and U. Maschke. Experimental investigation and modeling attempt on the effects of ultraviolet aging on the fatigue behavior of an ldpe semi-crystalline polymer. *International Journal of Fatigue*, 142:105952, 2021.

E. H. Lee. Elastic-plastic deformation at finite strains. 1969.

K. Loeffel, L. Anand, and Z. M. Gasem. On modeling the oxidation of high-temperature alloys. *Acta Materialia*, 61(2):399–424, 2013.

K. N. Long, T. F. Scott, H. J. Qi, C. N. Bowman, and M. L. Dunn. Photomechanics of light-activated polymers. *Journal of the Mechanics and Physics of Solids*, 57(7):1103–1121, 2009.

M. F. Modest and S. Mazumder. *Radiative heat transfer*. Academic press, 2021.

H. Mohammadi, V. Morovati, A.-E. Korayem, E. Poshtan, and R. Dargazany. Constitutive modeling of elastomers during photo-and thermo-oxidative aging. *Polymer Degradation and Stability*, 191:109663, 2021.

A. Najmeddine and M. Shakiba. Physics and chemistry-based phase-field constitutive framework for thermo-chemically aged elastomer. *International Journal of Mechanical Sciences*, 262:108721, 2024.

A. Najmeddine, Z. Xu, G. Liu, Z. L. Croft, G. Liu, A. R. Esker, and M. Shakiba. Physics and chemistry-based constitutive modeling of photo-oxidative aging in semi-crystalline polymers. *International Journal of Solids and Structures*, 239:111427, 2022.

H. Nakajima, P. Dijkstra, and K. Loos. The recent developments in biobased polymers toward general and engineering applications: Polymers that are upgraded from biodegradable polymers, analogous to petroleum-derived polymers, and newly developed. *Polymers*, 9 (10):523, 2017.

S. Narayan and L. Anand. Fracture of amorphous polymers: A gradient-damage theory. *Journal of the Mechanics and Physics of Solids*, 146:104164, 2021.

Z. Pan and L. Brassart. Constitutive modelling of hydrolytic degradation in hydrogels. *Journal of the Mechanics and Physics of Solids*, 167:105016, 2022. ISSN 0022-5096. doi: https://doi.org/10.1016/j.jmps.2022.105016. URL `https://www.sciencedirect.com/science/article/pii/S0022509622002010`.

Z. Pan, H. Chen, and L. Brassart. Constitutive modelling of hydrolytic degradation and viscoplasticity in glassy polymers: An effective temperature approach. *International Journal of Plasticity*, page 104690, 2026.

D. Rasselet, A. Ruellan, A. Guinault, G. Miquelard-Garnier, C. Sollogoub, and B. Fayolle. Oxidative degradation of polylactide (pla) and its effects on physical and mechanical properties. *European Polymer Journal*, 50:109–116, 2014.

T. Sain, K. Loeffel, and S. Chester. A thermo–chemo–mechanically coupled constitutive model for curing of glassy polymers. *Journal of the Mechanics and Physics of Solids*, 116: 267–289, 2018.

M. Shakiba and A. Najmeddine. Physics-based constitutive equation for thermochemically aged elastomers based on crosslink density evolution. *Journal of Mechanics of Materials and Structures*, 17(3):229–246, 2023.

M. N. Silberstein, K. Min, L. D. Cremar, C. M. Degen, T. J. Martinez, N. R. Aluru, S. R. White, and N. R. Sottos. Modeling mechanophore activation within a crosslinked glassy matrix. *Journal of Applied Physics*, 114(2), 2013.

N. Singh, O. A. Ogunseitan, M. H. Wong, and Y. Tang. Sustainable materials alternative to petrochemical plastics pollution: A review analysis. *Sustainable horizons*, 2:100016, 2022.

H. Song and Z. Zhong. Nonlinear constitutive model of cfrp composites under constant direct current: Combined effects of thermal damage and dielectric degradation. *Journal of the Mechanics and Physics of Solids*, 184:105547, 2024.

V. Srivastava, S. A. Chester, N. M. Ames, and L. Anand. A thermo-mechanically-coupled large-deformation theory for amorphous polymers in a temperature range which spans their glass transition. *Int. J. Plast.*, 26(8):1138–1182, aug 2010. ISSN 0749-6419. doi: 10.1016/J.IJPLAS.2010.01.004.

H. Van Melick, L. Govaert, and H. Meijer. On the origin of strain hardening in glassy polymers. *Polymer*, 44(8):2493–2502, 2003.

S. Venkatesan and S. Basu. Investigations into crazing in glassy amorphous polymers through molecular dynamics simulations. *Journal of the Mechanics and Physics of Solids*, 77:123–145, 2015.

Y. Vidavsky, S. J. Yang, B. A. Abel, I. Agami, C. E. Diesendruck, G. W. Coates, and M. N. Silberstein. Enabling room-temperature mechanochromic activation in a glassy polymer: synthesis and characterization of spiropyran polycarbonate. *Journal of the American Chemical Society*, 141(25):10060–10067, 2019.

A. C. Vieira, R. M. Guedes, and V. Tita. Constitutive modeling of biodegradable polymers: Hydrolytic degradation and time-dependent behavior. *International Journal of Solids and Structures*, 51(5):1164–1174, 2014.

J. Wu and C. Buckley. Plastic deformation of glassy polystyrene: a unified model of yield and the role of chain length. *Journal of Polymer Science Part B: Polymer Physics*, 42 (11):2027–2040, 2004.

E. Yousif and R. Haddad. Photodegradation and photostabilization of polymers, especially polystyrene. *SpringerPlus*, 2(1):1–32, 2013.

Y. Zhu, C. Romain, and C. K. Williams. Sustainable polymers from renewable resources. *Nature*, 540(7633):354–362, 2016.

# A Uniaxial experiments preliminaries

We define the standard engineering[6] kinematic quantities for a uniaxial test, where the engineering strain is defined by

$$\varepsilon = \frac{l - l_0}{l_0} = \frac{u + l_0 - l_0}{l_0} = \frac{u}{l_0}\,, \tag{47}$$

where $l$ is the instantaneous gauge length, $l_0$ is the initial gauge length, and $u$ is the crosshead displacement; and the engineering strain rate is given by

$$\dot{\varepsilon} = \frac{\dot{u}}{l_0}\,, \tag{48}$$

where $\dot{u}$ is the crosshead velocity. Additionally, the engineering stress $P$, can be easily obtained by dividing the force over the initial cross-sectional area $A_0$, that is measured for each sample prior to testing

$$P = \frac{F}{A_0}\,. \tag{49}$$

We additionally define the standard true kinematic quantities for a uniaxial test, where the true strain is given by

$$\epsilon = \ln\left(\frac{l}{l_0}\right) = \ln\left(\frac{l_0 + u}{l_0}\right) = \ln\left(1 + \frac{u}{l_0}\right) = \ln(1 + \varepsilon)\,, \tag{50}$$

where $l$ is the instantaneous gauge length, $l_0$ is initial gauge length, $u$ is the displacement, and $\varepsilon$ is the engineering strain introduced in (47). Moreover, we introduce the term stretch $\lambda \overset{\text{def}}{=} \frac{l}{l_0}$. Additionally, assuming homogeneous deformation and incompressibility,[7] the true

[6] We use the terms "engineering" and "nominal" interchangeably; that is to refer to quantities defined in (47) for strain and (49) for stress.

[7] The incompressibility assumption is reasonable since the elastic deformation is small compared to the plastic deformation.

stress $\sigma$, can be easily obtained by

$$\sigma = \frac{F}{A}\,, \qquad \text{where} \qquad A = \frac{A_0}{\lambda}\,. \tag{51}$$

And thus (51) can be recast as

$$\sigma = \frac{F}{A_0}\lambda = P\lambda\,. \tag{52}$$